A comprehensive three-dimensional radiative magnetohydrodynamic simulation of a solar flare

M. C. M. Cheung [1,2,9]*, M. Rempel[3,9], G. Chintzoglou[1,4], F. Chen[3], P. Testa[5], J. Martínez-Sykora[1,6], A. Sainz Dalda[1,2,6], M. L. DeRosa[1], A. Malanushenko[3], V. Hansteen[1,7,8], B. De Pontieu[1,7], M. Carlsson[7,8], B. Gudiksen[7,8] and S. W. McIntosh[3]

Solar and stellar flares are the most intense emitters of X-rays and extreme ultraviolet radiation in planetary systems[1,2]. On the Sun, strong flares are usually found in newly emerging sunspot regions[3]. The emergence of these magnetic sunspot groups leads to the accumulation of magnetic energy in the corona. When the magnetic field undergoes abrupt relaxation, the energy released powers coronal mass ejections as well as heating plasma to temperatures beyond tens of millions of kelvins. While recent work has shed light on how magnetic energy and twist accumulate in the corona[4] and on how three-dimensional magnetic reconnection allows for rapid energy release[5,6], a self-consistent model capturing how such magnetic changes translate into observable diagnostics has remained elusive. Here, we present a comprehensive radiative magnetohydrodynamics simulation of a solar flare capturing the process from emergence to eruption. The simulation has sufficient realism for the synthesis of remote sensing measurements to compare with observations at visible, ultraviolet and X-ray wavelengths. This unifying model allows us to explain a number of well-known features of solar flares[7], including the time profile of the X-ray flux during flares, origin and temporal evolution of chromospheric evaporation and condensation, and sweeping of flare ribbons in the lower atmosphere. Furthermore, the model reproduces the apparent non-thermal shape of coronal X-ray spectra, which is the result of the superposition of multi-component super-hot plasmas[8] up to and beyond 100 million K.

Due to the complex, multiscale nature of the system, existing models of solar flares and eruptions treat aspects of the problem in a piecemeal manner. For instance, one-dimensional (1D) hydrodynamic loop models of flares[9,10] do not self-consistently take into account the evolving three-dimensional (3D) coronal magnetic field and associated energy conversion primarily by means of work done on the plasma by the Lorentz force of retracting field lines[11]. Similarly, two-dimensional[12] and 3D[13,14] magnetohydrodynamics (MHD) flare models neglect many important processes that determine the coupling between the corona, lower solar atmosphere and turbulent flows in the convection zone. As a result of the limiting assumptions of existing simulations, many aspects of how flares or eruptions are triggered, or how magnetic energy conversion occurs, remain speculative. Here, we present a comprehensive 3D radiative MHD simulation that (1) treats magnetic flux emergence and

eruption with a magnetic field geometry that mimics an observed active region, (2) includes the treatment of most of the physical processes considered essential to account for the bulk evolution of the mass density and energy in flares, and (3) yields remote sensing observables that are compatible with observational signatures of solar flares.

The setup of the simulation was inspired by the observed evolution of National Oceanic and Atmospheric Administration (NOAA) Active Region 12017. During its appearance on the visible disk of the Sun in late March and early April 2014, Active Region 12017 produced a series of soft X-ray flares with the following Geostationary Operational Environmental Satellites (GOES) flare classifications: one X-class, three M-class and about two-dozen C-class flares. Observational studies suggest that the flares were driven or triggered by the emergence of a parasitic bipolar magnetic region north of the pre-existing leading sunspot of Active Region 12017 (refs [15,16]). This work gives theoretical grounding to the plausibility of this scenario, but is not intended to model a specific flare of Active Region 12017. We used the MPS/University of Chicago Radiative MHD (MURaM) code, which treats magnetoconvection in the solar interior together with 3D radiative transfer in the photosphere. This code was recently extended to treat coronal physics in the form of optically thin radiative losses and field-aligned thermal conduction[17] (see Methods for details).

The simulation domain captures the top 7,500 km of the solar convection zone and the first 41,600 km of the overlying atmosphere. The initial setup consists of a bipolar sunspot pair, each with a magnetic flux of 3.4×10^{21} Mx. A strongly twisted magnetic bipole with 10^{21} Mx flux is emerged in proximity to one of the pre-existing sunspots. The emergence of the parasitic bipole leads to the creation of a twisted coronal flux rope well before flare onset[5,18,19]. Magnetic reconnection across multiple domains of connectivity changes the magnetic topology of the field, facilitating rapid energy release. Details of how the magnetic field evolves before, during and after the flare are given in the Methods.

Our numerical simulation has the relevant physics (including 3D MHD, radiative transfer and thermal conduction; see Methods) required to model the system from flux emergence to eruption, and for synthesizing realistic remote sensing observables. The observables most routinely measured and used for studying flares are X-ray fluxes in the 1.0–8.0 Å (solid red) and 0.5–4.0 Å (dashed blue) wavelength bands measured by NOAA's GOES. Synthetic
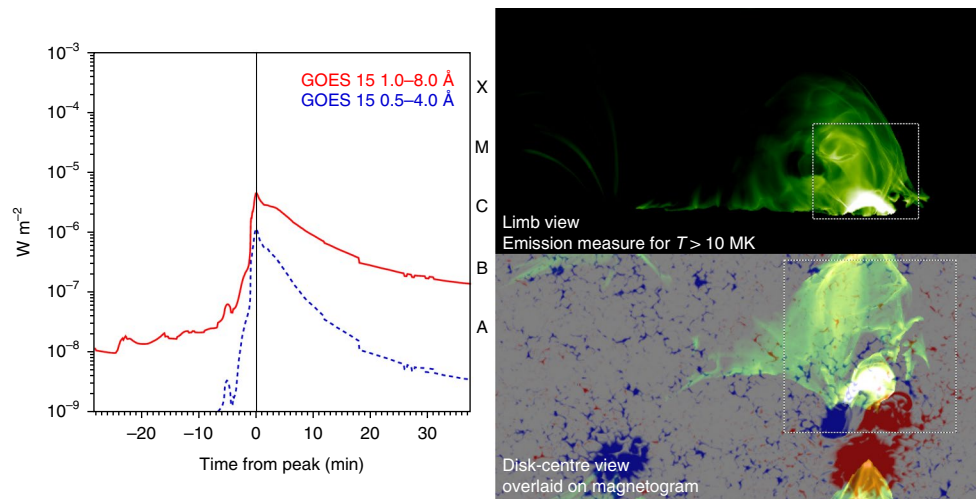
Fig. 1 | Synthetic X-ray flux time profiles and associated hot plasma. Left: synthetic time profiles of X-ray fluxes as would be measured by the long- (1.0–8.0 Å, solid red) and short-wavelength (0.5–4.0 Å, dashed blue) X-ray channels of the GOES 15 satellite. The corresponding NOAA flare class designation is indicated on the right by the letters A, B, C, M and X. The peak flux in the long-wavelength channel gives a GOES flare classification of C4. Right: simulated disk-centre (bottom; overlaid on a magnetogram) and limb views (top; emission measure of plasma with $T \geq 10$ million K, shown with increasing values as black < green < white) of flare plasma at the time ($t=0$) during the peak of the X-ray flux. The hottest loops connect the opposite polarities of the parasitic bipolar emerging flux region north of the negative (red) polarity sunspot. These loops are heated by the energy released by the strong magnetic fields that have undergone reconnection. The dashed boxes in the disk-centre and limb view panels indicate the regions shown in Figs. 2 and 3, respectively.

X-ray fluxes are shown in the left panel of Fig. 1. As is typical of real observed flares, the synthetic light curve shows an impulsive rise in both profiles over a time scale of a few minutes, followed by a gradual decay spanning tens of minutes. The peak flux in the 1–8 Å wavelength band (which, by our definition, occurs at $t=0$) yields a GOES flare classification of C4. The impulsive 100-fold increase in the X-ray flux over the quiescent background occurs as the result of chromospheric evaporation filling the coronal loops with high-temperature, high-emission-measure plasma. The rise time of the X-ray flux is comparable to the timescale for chromospheric evaporation to fill the loops. We find blue shifts due to evaporation for temperatures of a few tens of millions of K (see Fig. 2). The corresponding upflow speeds of 300 km s^{-1} reach a significant fraction of the speed of sound at 10 million K (about 470 km s^{-1}). For a 10 Mm loop, this gives a characteristic time scale of 30 s.

The right panel of Fig. 1 shows the state of the model flare at peak flare time. The top-down view (bottom) shows how a compact set of flare loops connect opposite-polarity spots in the parasitic emerging flux region. The limb view (top; line of sight along the y axis) reveals a set of diffuse loops, with complex morphology reminiscent of twisted flux ropes[20,21], reported in eruptive flares observed in the hot channels (for example, 131 Å) of the Atmospheric Imaging Assembly (AIA) onboard the Solar Dynamics Observatory (SDO).

The peak of the GOES X-ray flux occurs as a result of chromospheric evaporation filling up flare loops with hot plasma—an effect previously studied only in simplified 1D and two-dimensional models[9,12,22,23]. In this simulated flare, the energy released by reconnection and magnetic field retraction is primarily transported from the corona to the chromosphere by thermal conduction, as opposed to alternative mechanisms such as energetic electron beams or Alfvén waves[24]. While we do find Alfvénic pulses that are triggered by the flare reconnection, they do not contribute significantly to the net energy transport (magnetic energy release in the lowermost 3 Mm above the photosphere is less than 10% of the energy transported there through conduction). The conductive energy flux reaches values of up to 3×10^{11} erg cm^{-2} s^{-1} near the flare ribbons, which is comparable to the non-thermal energy fluxes required in detailed 1D models of flare ribbons[25].

The top panel of Fig. 2 shows, for a top-down view, synthetic emission-measure-weighted Doppler velocity maps for plasma at temperatures of $T=1$, 10 and 25 million K near the peak of the flare. The Doppler velocities as a function of the temperature sampled at three flare loop footpoints are shown in the lower panel of the figure. A feature common to these evaporation profiles is the reversal of the sign of Doppler velocity at roughly a few million K. At low coronal and transition region temperatures ($T \lesssim 5$ million K), the plasma has downflow (redshifted Doppler) velocities of the order of tens of km s^{-1}. At hotter temperatures, the plasma is flowing up at hundreds of km s^{-1}. The specific temperature at which the reversal from downflow to upflow occurs changes dynamically on time scales of the order of seconds (see an animated version of Fig. 2 in Supplementary Video 1) due to the impulsive nature of the energy deposition and the superposition of emission from plasma evaporating along stacked flare loops. The trend is robust across multiple loops in the flare arcade, in agreement with extreme ultraviolet (EUV) spectrograph observations[26,27].

In the Methods, we show that non-Gaussian (κ) distributions of EUV emission-line profiles can arise due to temperature and velocity gradients along the line of sight. Such profiles have previously been taken as evidence for microscopic physical processes such as heavy-ion acceleration[28]. This work suggests that κ distributions of EUV lines are due to (macroscopic) MHD structuring in solar flares and, by extension, other astrophysical sources.

In the simulation, we identified a coronal dimming region away from the main flare arcade. In synthetic AIA EUV images (see Methods), the dimming appears in the 94, 193 and 335 Å channels, and is most prominent in the 211 Å channel. The dimming occurs due to strong heating of plasma on magnetic field lines that have undergone reconnection. Due to periodic side boundary conditions in the model, the magnetic connectivity of the modelled dimming region may not be representative of coronal dimming regions on the Sun. Nevertheless, it is worth reporting that a single model produces both a flare and dimming.

A synthetic X-ray spectrum (see Fig. 3; an animated version is available as Supplementary Video 2) computed with thermal bremsstrahlung (the two peaks below 10 keV are emission lines) roughly
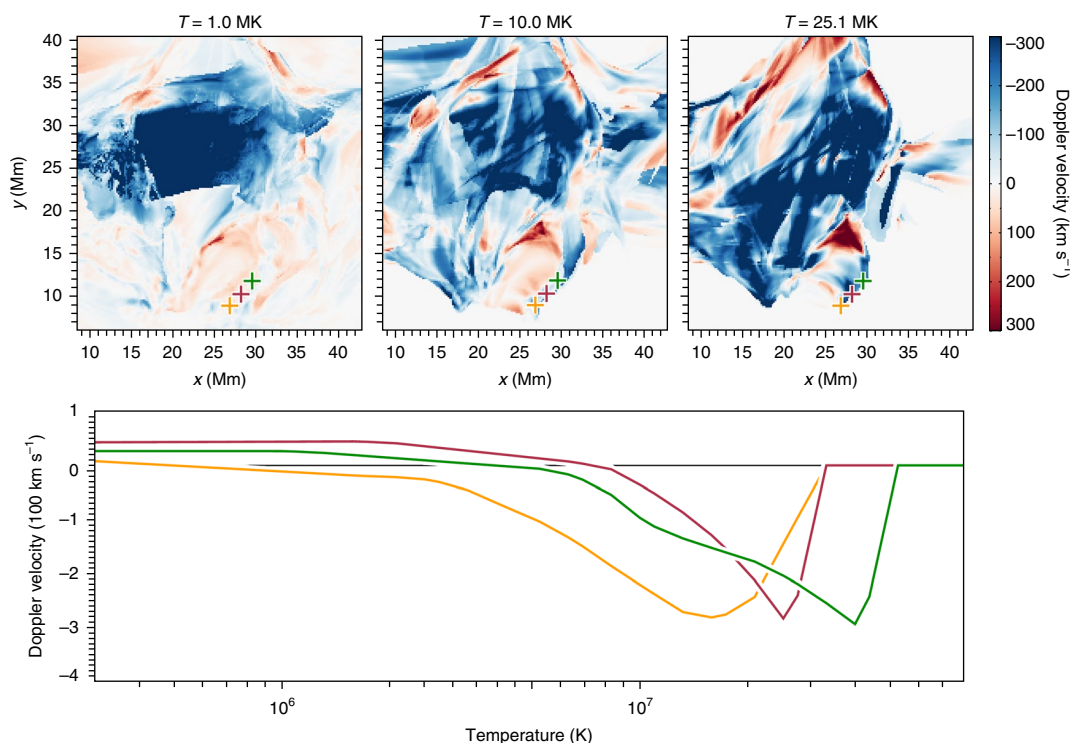
Fig. 2 | Doppler velocity maps and velocity profiles for plasma at various temperatures. Top: Doppler velocity maps for plasma at (left to right) $T = 1.0$, 10.0 and 25.1 million K near the peak ($t = -8$ s) of the simulated flare. The maps are scaled between ± 300 km s^{-1} with blue showing upflows and red showing downflows. Bottom: velocity profiles as functions of the plasma temperature, sampled at the positions indicated by crosses in the upper panels (positive values show downflows, negative values show upflows). Velocity profiles sampled at the footpoints show evaporation profiles with upflows of ~500 km s^{-1} at $T \geq 10$ million K. The field of view displayed in the top panels and used to generate the results in the bottom panel is shown as a dashed box in Fig. 1 (bottom right panel). An animation version of this figure is available as Supplementary Video 1.

follows a power-law profile. Power-law profiles for solar flare X-ray spectra with photon energy $E_{ph} \gtrsim 10$ keV are often taken as evidence for the existence of an energetically important non-thermal particle population[29,30]. However, the power-law spectrum in this model is due solely to spatial inhomogeneities (both transverse and parallel to the line of sight) in temperature and emission measure. It is the result of multithermal plasma (see the emission-measure curve in the top panel of Fig. 3) spontaneously generated by the plasma adjusting to the relaxation of the magnetic field. The release of magnetic energy powers adiabatic compression and viscous dissipation, which yields super-hot plasma with temperatures exceeding 100 million K. This thermal emission is, in this simulation, the sole source of the hard X-rays ($E_{ph} > 25$ keV; red contours in Fig. 3) located at a higher altitude than the soft X-ray ($6 \leq E_{ph} \leq 12$ keV; blue contours) and EUV loop tops (for example, the 94 Å channel of the SDO/AIA).

The 3D MHD model of a flaring active region presented in this paper successfully reproduces many properties of flare observations. These include the spectral distributions of X-ray emission, the high-energy tail of which is typically interpreted as originating from non-thermal particles. This model, which does not include the effects of non-thermal particles, shows that it is possible to interpret a number of observational aspects of flares as arising from thermal processes involving energy release locally in the corona, and subsequent thermal conduction and radiation. We highlight the importance of combining high-resolution observations with radiative MHD simulations to distil relevant physical insights from remote sensing measurements, with implications for the interpretation of ultraviolet, EUV and X-ray spectra from astrophysical sources. We note that this good agreement of course does not exclude the relevance of non-thermal particles for some flare phenomena, but

merely shows that their role might be, in principle, more limited than usually assumed. In the future, a model including all physical effects will be required to diagnose the relative importance of kinetic versus MHD effects in flares.

Methods

We used the extended version of the MURaM radiative MHD code[17], which includes coronal physics in terms of field-aligned heat conduction and optically thin radiative losses. Stringent time-step constraints arising from the high coronal Alfvén velocity, as well as high thermal conductivity, were avoided through the use of the Boris correction[31,32] and hyperbolic heat conduction[33,34]. These approximations are inspired by semi-relativistic physics and impose a maximum propagation speed for Alfvén waves and temperature fronts through a 'reduced speed of light', c. We dynamically adjusted c by choosing $c = \max(2C_S, 3|v|)$, where C_S denotes the ion speed of sound and $|v|$ the flow velocity. This led to cut-off speeds on the order of 1,000 km s^{-1} for quiescent corona. During the flare, we found advection speeds of up to 4,000 km s^{-1} and, consequently, c was raised during this dynamic phase to values of 12,000 km s^{-1}. We conducted an additional control experiment (C1; described below) in which we used a three-times-larger value for c (more than 10% of the true speed of light) and found comparable results. In addition, we saturated the conductive heat flux at one-sixth of the electron-free streaming limit[9], which essentially limited the peak transport velocity due to conduction to $2C_S$—a value that is well captured by our choice of c.

For this model, we added the following modifications to the numerical diffusivities. We applied the piecewise linear reconstruction in the slope-limited diffusion scheme, as well as additional fourth-order hyperdiffusion to $\log[\varepsilon]$ instead of ε, where $\varepsilon = E_{int}/\rho$. This change prevents numerical problems (overshoots and undershoots) near the flare ribbons, where gradients of ε can be significant. In addition, we added a 'coronal mass ejection mode' that is enabled in regions with cool mass ejecta. When $|v| > \sqrt{C_S^2 + V_A^2}$, ($V_A$ denotes the Alfvén velocity) we used a more diffusive setting for all hydrodynamic variables (see refs [17,35] for further details on the treatment of numerical diffusivity).

Simulation domain and boundary conditions. We consider a simulation domain spanning ± 49.152 and ± 24.576 Mm in the horizontal x and y directions, respectively. In the vertical (z) direction, the computational domain spans from
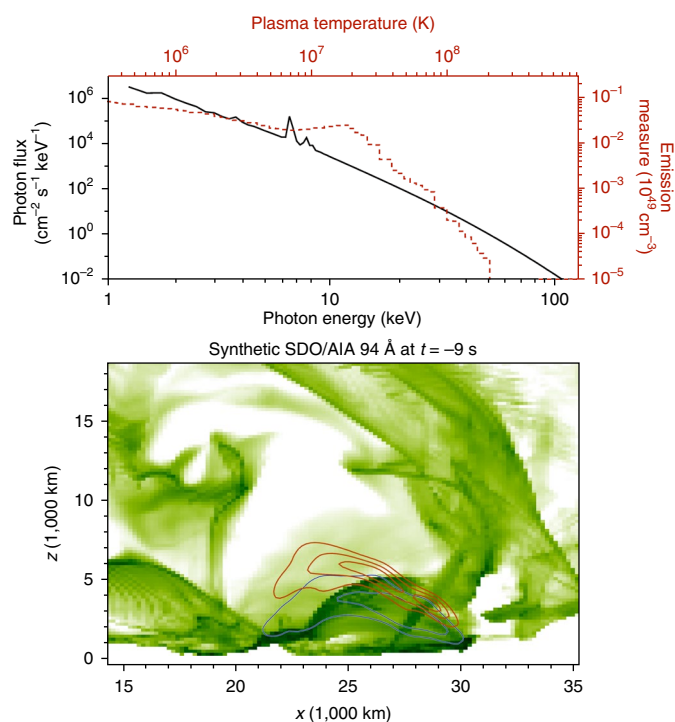
Fig. 3 | Synthetic X-ray spectrum and EUV/X-ray emission maps at t = −9 s. Top: X-ray spectrum at t = −9 s, synthesized assuming thermal bremsstrahlung from the underlying multithermal emission-measure distribution of the simulated flare. Bottom: corresponding emission maps. The blue contours outline the location of the soft X-ray source ($6 \leq E_{ph} \leq 12$ keV) at levels of 400 and 800 photons cm^{-2} s^{-1}. The red contours show the super-hot, coronal hard X-ray source ($E_{ph} \geq 25$ keV at fluxes of 0.1, 0.2 and 0.3 photons cm^{-2} s^{-1}) above the soft X-ray and EUV loop tops. The green shading shows a synthetic image of the SDO/AIA 94 Å channel. The field of view shown in the bottom panel is indicated as a dashed box in Fig. 1 (top right panel). An animated version of this figure is available as Supplementary Video 2.

7.5 Mm beneath to 41.6 Mm above the photosphere. The grid spacing is 192 km in the horizontal and 64 km in the vertical direction. Horizontal boundary conditions are periodic. The bottom boundary is open and allows convective energy transport across the domain boundary in regions with a vertical magnetic field strength of l magnetic field strength of $|B_z| < 5$ kG. In regions with stronger field, the velocity at the boundary is set to zero to prevent a rapid decay of the pre-existing bipolar group. The open boundary is implemented through a mirroring of the three mass flux components into the boundary cells, fixed mean gas pressure with damped pressure perturbations and fixed inflow entropy, whereas the outflow entropy is mirrored into the boundary cells[35]. To allow for flux emergence, this boundary condition is temporarily replaced by the flux-emergence boundary condition described below. At the top boundary, the magnetic field is matched to a potential field extrapolation that is computed from the vertical magnetic field at the uppermost domain layer, and vertical flows are allowed but strongly damped to ensure numerical stability (the vertical mass flux is mirrored into the ghost cells; its value in the first ghost cell is reduced by a factor of 2; its value in the second ghost cell is reduced by a factor of 4). The conductive heat flux is set to zero at the top boundary.

Initial-state and flux-emergence (FEM) setup. The initial setup consists of a bipolar group with two sunspots of 3.4×10^{21} Mx flux that are positioned at the (x, y) coordinates of (−24.576, 0) Mm and (+24.576, 0) Mm for the positive and negative polarities, respectively. The simulation was evolved with this setup for a few hours until a thermally relaxed corona with an average temperature of about 2 million K was reached (see ref. [17] for further details on this setup). At the bottom boundary ($z = −7.5$ Mm), we imposed the emergence of an additional strongly twisted bipolar flux system centred at $(x_c, y_c) = (24.576, 6.984)$ Mm. We defined an ellipsoidal flux-emergence region with the major axes $(a, b) = (10, 2.8)$ Mm:

$$F(x, y) = 1 - \left(\frac{x - x_c}{a}\right)^2 - \left(\frac{y - y_c}{b}\right)^2 \geq 0 \qquad (1)$$

within which we imposed for $T_{FEM} = 10,000$ s an upflow of $v_{FEM} = 200$ m s^{-1}. Within the flux-emergence region $F(x, y) \geq 0$, we imposed a horizontal magnetic field (B_x, B_y) as a function of time (we assumed $t = 0$ s was the start of the flux emergence):

$$B_x(x, y, t) = B_0 F(x, y) \sin(\pi t / T_{FEM}) \qquad (2)$$

$$B_y(x, y, t) = B_0 \lambda F(x, y) \sin(2\pi t / T_{FEM}) \qquad (3)$$

with the parameters $B_0 = 20$ kG and $\lambda = −2$. This led to the emergence of a bipole with the same x-directed orientation as the pre-existing active region and a right-handed twist. The total amount of horizontal flux crossing the bottom boundary in the flux-emergence region is given by:

$$\Phi_{FEM} = \frac{8}{3\pi} B_0 v_{FEM} T_{FEM} b = 9.5 \times 10^{20} \text{ Mx} \qquad (4)$$

that is, about 28% of the pre-existing active region flux. We did not impose any vertical magnetic field in the flux-emergence region, since B_z is computed self-consistently from the induction equation and the $\nabla \cdot \mathbf{B} = 0$ constraint. Before and after the flux emergence, we made a smooth transition between flux emergence and open boundary conditions over a time scale of 1,000 s to avoid sharp transients in the vertical velocity. The flux emergence in the photosphere starts with a delay of about 3 h, and the flare happens about 3.5 h after the start of photospheric flux emergence.

An example of an observed active region with parasitic bipole emergence. The simulation in this study is not intended to model a specific flare of an observed active region, but was inspired by an example of a flare-productive active region with parasitic bipole emergence into a pre-existing sunspot in NOAA Active Region 12017. On 2014 March 29, the region produced what is arguably the best-observed X-class flare by virtue of a coordinated observing campaign that directed several ground-based and space-borne observatories to observe the region on that day[15,16,25,36–40]. In addition to the X1 flare, the active region produced three M-class and about two-dozen C-class flares over the course of its passage across the solar disk. The strongest flares occurred during the emergence of a parasitic bipole immediately north of the leading polarity spot (see Supplementary Fig. 1).

We emphasize here that our simulation does not use observed magnetograms for constraining the evolution of the actual Active Region 12017. Rather, the approach was to reduce the system to its essential elements (emergence of a parasitic bipole into the leading polarity of a pre-existing active region) without neglecting important physical processes. One difference between the model and Active Region 12017 is that periodic side boundary conditions were used in the simulation, whereas Active Region 12017 is relatively isolated from other active regions on the Sun. This would impact the amount of free energy and helicity that can accumulate in the twisted coronal flux rope before it erupts. However, this comprehensive 3D radiative MHD simulation of a flare still provides important insights about how the magnetic field is reconfigured and magnetic energy is released, and how this translates into flare observables.

Magnetic configurations before, during and after the flare. The morphological evolution of the coronal loops, as shown in Supplementary Fig. 1, suggests that the flare is preceded by magnetic reconnection between two magnetic subdomains (field lines connecting the pre-existing sunspot pair, and field lines connecting the parasitic bipole) transferring magnetic flux above the flux rope to complementing subdomains (see Supplementary Video 3 for an animated version of Supplementary Fig. 1). Similarly, flux transfer between neighbouring subdomains is found to occur in the data-inspired MHD simulation before the flare. To quantify magnetic linkage/connectivity changes that occur during the simulated flare, we traced magnetic field lines and defined magnetic subdomains according to the locations of pairs of conjugate footpoints. For the following discussion, four magnetic subdomains are important (see Supplementary Fig. 2). Subdomain 1 (red) contains field lines connecting the parasitic bipole polarities. Subdomain 2 (green) contains lines connecting the positive parasitic polarity to the negative pre-existing polarity at the north of the field of view. Subdomain 3 (yellow) contains lines emanating from the negative pre-existing polarity to any positive polarity outside the parasitic bipole. Subdomain 4 (blue) contains lines connecting the negative parasitic polarity to pre-existing positive polarity flux.

At $t = −90$ min, we find a magnetic flux rope structure residing in the corona above the parasitic bipole (magenta volume rendering in Supplementary Fig. 2). The parasitic bipole results from the emergence of a twisted flux rope. Although an idealized twisted flux rope was imposed to kinematically rise through the bottom boundary of the domain (see the Methods section 'Simulation-domain boundary conditions' for details), the flux rope does not rise through the domain in a kinematic fashion such as in idealized MHD models that exclude the upper convection zone[41]. This is due to the strong stratification (the density contrast between the bottom boundary and photosphere is 10^3) and interaction with convective flows. Emergence into the tenuous atmosphere leads to Lorentz-force-driven horizontal shear flows and the formation of a compact magnetic polarity inversion line, where tether cutting and flux cancellation occur to form a new

coral flux rope[18,42]. This model shares some similarity with NOAA Active Region 12017 in that force-free field extrapolations[7,37,40] from photospheric vector magnetograms of the active region also contain a coronal flux rope above the polarity inversion line of the observed parasitic bipole.

In the simulation, the pre-existing flux rope is initially contained within subdomain 1. At $t = -25$ min, the overlying flux (shown as red field lines in Supplementary Fig. 2) begins to gradually reconnect with magnetic flux of subdomain 3 (black arrows), thereby transferring flux to subdomains 2 and 4 (white arrows). By $t = -5$ min, most of the flux overlying the flux rope has reconnected, and the more twisted field lines in the flux tube now start reconnecting with the flux from subdomain 3, as shown in Supplementary Fig. 3a. This leads to an increase in the rate of reconnection, resulting in temperatures reaching and exceeding 100 million K (as rendered in cyan in Supplementary Fig. 3a) and a corresponding increase in the soft X-ray flux, as shown in Supplementary Fig. 3e.

The flux removed from subdomains 1 and 3 is re-partitioned to (1) a hot post-flare loop arcade (subdomain 2) oriented in the y direction and (2) some overlying flux in subdomain 4. During this faster reconnection phase, the maximum amount of flux transferred from subdomains 1 and 3 to subdomains 2 and 4 is 4×10^{20} Mx (~19% of the total parasitic flux content). Over time, due to the continuous pile-up of the y-directed flux, the magnetic pressure in subdomain 2 gradually increases (green lines in Supplementary Fig. 3b). This accumulation of flux occurs during both the earlier, slower ($-25 < t < -5$ min) and later, more rapid ($t > -5$ min) reconnection phases. As a result, a secondary rotational discontinuity is generated between subdomain 2 and the subdomain 4 flux, which now overlies the post-flare arcade (blue lines in Supplementary Fig. 3c). This transfers flux into (1) a long hot loop system connecting the pre-existing negative sunspot to pre-existing positive polarity flux (that is, subdomain 3) and (2) post-flare loops anchored at the parasitic polarities (orange loops in subdomain 1; rooted at ribbons shown in the animated version of Supplementary Fig. 5). By this stage, the reconnection rate between subdomains 1 and 3 has drastically decayed and the flare's late phase is dominated by the steady reconnection between subdomains 2 and 4 transferring flux back to subdomain 3 (footpoints of remote brightenings away from the sunspots) and to subdomain 1 (post-flare loop arcade in parasitic bipole; Supplementary Fig. 3d). In the aftermath of the flare, the four subdomains have recovered much of their pre-flare flux content. The twisted field lines associated with the flux rope have been removed and, consequently, the free energy has decreased by 5×10^{30} erg, which is about 10% of the total free energy stored in the corona. After a flux rope has formed and is destabilized, the overall topological evolution of the system is consistent with the 3D magnetic breakout scenario[6,43,44]. In this model, the twisted flux rope is formed by shearing and magnetic cancellation driven by flux emergence[5,18,19,45]. Here, we focus on the remote sensing observables that occur as the result of a flux rope eruption. Determining the precise mechanism responsible for the destabilization of the simulated flux rope requires a careful, detailed analysis of the evolving magnetic configuration[40,46], which is beyond the scope of our present investigation. An alternative illustration of the dynamics of the magnetic evolution using representative field lines (coloured after each subdomain) is shown in Supplementary Fig. 4.

Supplementary Fig. 5a presents a synthetic magnetogram corresponding to the warped $\tau = 0.1$ (where τ is the optical depth) surface. Horizontal magnetic field changes in the lower chromosphere (700 km height above the horizontal layer where $\langle \tau \rangle = 1$) are shown in Supplementary Fig. 5b. Supplementary Fig. 5c–f shows synthetic SDO/AIA emission, with the AIA 171 Å channel in the left panels and the AIA 94 Å channel in the right panels. Supplementary Fig. 5c,d shows a top view, while Supplementary Fig. 5e,f shows a side view along the y direction. The presented snapshot corresponds to the flare peak as defined by the soft X-ray emission in Fig. 1. Owing to horizontal periodicity, we shifted the domain such that the pre-existing active region (Supplementary Fig. 5a) appears on the edges of the domain. An animation of Supplementary Fig. 5 covers the evolution over a 66 min interval starting 28 min before the flare. Supplementary Fig. 5c highlights the position of flare ribbons. White arrows in Supplementary Fig. 5c point to flare ribbons that are connected to the reconnection site that is shown in Supplementary Fig. 4b. The red arrow in Supplementary Fig. 5c points towards the footpoints of the post-flare arcade that is shown Supplementary Fig. 4c,d. The flare ribbons are also the regions with the strongest changes in the horizontal field strength in Supplementary Fig. 5b. Starting from about 3 min before the flare peak, the AIA 94 Å channel shows a dimming (the dimming also appears in 193 and 335 Å, and is the most prominent in the 211 Å channel) that is caused by strong heating of field lines that connect the reconnection site shown in Supplementary Fig. 4b to the flare ribbons highlighted by white arrows in Supplementary Fig. 5c. In Supplementary Fig. 5e, we highlight the low-lying post-flare loops that are also a strong source of soft X-ray emission (Fig. 1). The flare leads to a mass ejection highlighted in Supplementary Fig. 5e.

Control experiments. Here, we present numerical simulations of a solar flare that are based on a series of approximations in the numerical treatment. We use single-fluid MHD and assume a thermal plasma with temperatures reaching 500 million K. We use semi-relativistic MHD with a reduced speed of light to limit Alfvén and heat conduction speeds. To assess whether any of these

assumptions influence the results presented here, we conducted a series of control experiments. While the validity of MHD does not depend on whether a plasma is thermal or not, the computation of temperature (entering heat flux and radiative loss), as well as pressure, is based on that assumption. In addition, reconnection is enabled by numerical magnetic diffusivity, which is strongly resolution dependent. We conducted three additional control experiments. In experiment C1, we increased the peak Alfvén velocity (that is, the 'reduced speed of light') by a factor of 3 by choosing $c = 3\max(2C_S, 3|v|)$. In the control experiment C2, we used the increased peak Alfvén velocity from C1 and also lifted the saturation heat flux by a factor of 100. The control experiment C3 used the same setup as our reference case, but a resolution increased by a factor of 1.5 in all 3 grid directions. Perhaps the most notable points are the following. In the control experiments C1 and C2, the conductive heat flux played a stronger role in balancing the magnetic energy release in the corona. As a consequence, the energy that was transported by the advective energy flux into the upper part of the domain was reduced, leading to an overall cooler corona during the flare. However, there were no significant differences in the total energy released during the flare. Increasing resolution (C3) led to a delay of the flare by about 5 min, but no difference in the total released energy.

κ distributions of coronal emission lines. Spectral profiles of optically thin coronal emission lines of hot flaring plasma have been reported to be better described in terms of κ distributions[28]:

$$I_\kappa(\lambda) = B[0]\left(1 + \frac{(\lambda - B[1])^2}{2B[2]^2 B[3]}\right)^{-B[3]} \tag{5}$$

compared with Gaussian distributions:

$$I_G(\lambda) = A[0]\exp\left(-\frac{(\lambda - A[1])^2}{2A[2]^2}\right) \tag{6}$$

where A and B are free parameters. κ distributions could result from (1) microscopic, non-Maxwellian velocity distributions of accelerated heavy ions[28] and/or (2) thermal and velocity (that is, bulk plasma) variations along the line of sight. To test the validity of the second explanation, we synthesized spectral profiles[47] of the Fe XVI 262.976 Å line, degraded it to the spectral (25 km s^{-1}) and spatial (2″) of the Hinode EUV Imaging Spectrometer, and performed line fits using both κ and Gaussian distributions. For several plane-of-sky positions in the simulated flare, the κ distribution was found to provide a better fit to the synthetic, line-of-sight integrated emission profiles (see Supplementary Fig. 6 for two examples). Such profiles tend to be narrower at the peak and broader at the tails compared with Gaussian functions. The quality of the fit was quantified using chi-squared values $\left(\chi^2 = \Sigma_i \left(\frac{I(\lambda_i) - I_k(\lambda_i)}{\sigma_i(\lambda_i)}\right)^2\right)$ for signals larger than 2 data numbers per second, where we estimated σ_i assuming Poisson noise for a signal-to-noise ratio of 20. The difference in χ^2 values between Gaussian and κ function fits is in accordance with observations. This result suggests that the existence of κ distributions in coronal emission lines may not necessarily be evidence of certain microscopic physical processes (such as heavy-ion acceleration).

Effect of periodic boundary conditions. One major difference between the 3D MHD simulation in this study and active regions on the Sun is the imposed periodic side boundary conditions used in the simulation. To isolate the impact of periodic side boundary conditions on coronal field evolution for the magnetic geometry relevant to this setup, we carried out idealized experiments using a magnetofriction code[48,49], which does not treat the full dynamics of MHD (as is treated by the MURaM code) but does relax the coronal field in response to photospheric driving and the presence of Lorentz forces. In both magnetofriction experiments, the computational domain spans 98.3 Mm × 49.1 Mm in the horizontal directions, and 73.7 Mm in the vertical direction (from $z = 0$ at the photospheric level). The initial condition consists of a pair of opposite-polarity concentrations at the photosphere and a potential field in the corona. This is intended to mimic, to an idealized level, the pre-existing topology of the magnetic field in the MURaM MHD simulation.

From the initial condition, we imposed the kinematic emergence of an idealized twisted flux tube (by imposing the bottom boundary $\vec{E} = -\vec{v} \times \vec{B}$ electric field) just north of the negative polarity pre-existing flux concentration (that is, the leading 'sunspot'). The resulting model photospheric magnetogram is shown in Supplementary Fig. 7, where blue and red denote positive and negative polarity fields, respectively (see Supplementary Video 5 for an animated version).

We compared the following two simulations.

- Magnetofriction periodic experiment. Here, we used periodic side boundary conditions so the magnetic topology of this experiment was similar to that of the fully compressible MHD simulation of the flare.
- Magnetofriction enclosed experiment. Here, the side boundaries were perfectly conducting, so no magnetic flux penetrated through. In this case, the initial potential field and, thereafter, the current-carrying field were wholly

contained within the computational box. The field in this simulation had a markedly different magnetic topology from that of the magnetofriction enclosed experiment and the MHD flare simulation.

Supplementary Fig. 8 shows a side-by-side comparison between the two models with different side boundary conditions. The bottom panels show the top-down view, with the photospheric B_z field depicted in greyscale. The magnetic field lines are visualized by line-of-sight integration along a proxy emissivity cube, whose values are proportional to the field-line-averaged current density (j^2)[48]. This visualization method is designed to highlight magnetic loops that are undergoing magnetic reconnection or Lorentz relaxation after reconnection. The upper panels show the line-of-sight integral of this proxy emissivity for a 'limb' perspective.

The left and right halves of the animation show the magnetofriction periodic and enclosed runs, respectively. This comparative study reveals a number of common and uncommon features:

(1) Long-range magnetic loops and ribbons. As expected, the magnetofriction periodic run shows long-range loops that connect across the periodic side boundaries and have a connectivity similar to that of the periodic, radiative MHD flare simulation. In contrast, the magnetofriction enclosed case shows only loops on the upper half of the simulation domain (when looking down from a vantage point where $z > 0$). This is because the magnetic fields in this case cannot establish connectivity across the side boundaries. From this, one concludes that the locations of the long-range loops (length $L > d$, where d is the size of the parasitic bipole) are sensitive to boundary conditions.

(2) Compact flare loops confined to the parasitic bipole and pre-existing negative spot. Up to time $t = 200$ min, the morphology of the compact flare loops connecting the parasitic bipole and pre-existing negative spot is similar in both experiments. These features are due to reconnection of the parasitic bipole field with the canopy field of the neighbouring sunspot. Since the parasitic polarity emerges in the vicinity of the sunspot, the reconnection occurs at a relatively low height $\sim d$ and is not sensitive to the periodic or reflecting side boundary conditions. Beyond $t = 200$ min, the long-range flare loops and ribbon structure diverge between the two runs, as discussed in point (1).

(3) Magnetic energy evolution. The total magnetic energy in the two numerical experiments is plotted in Supplementary Fig. 9. The orange and red curves show the energy curves for the magnetofriction periodic and enclosed experiments, respectively. Due to the confinement of the field in the magnetofriction enclosed experiment, the total magnetic energy contained in the domain is consistently higher. The emergence of the parasitic bipole leads to the increase in magnetic energy in both runs. At $t = 160$ min, reconnection between the parasitic bipole field and sunspot canopy field allows the system to relax to a lower energy state. Since these are magnetofriction models, the relaxation of the field is slower than in an MHD simulation. Nevertheless, the decrease of the magnetic energy is comparable in both runs ($\sim 10^{31}$ erg). The similarity of the two energy curves (except for a background offset) is indicative of the fact that the energy decrease is predominantly due to the interaction between the strong magnetic fields close to the parasitic bipole and sunspot. This is also the region where the compact flare arcade and loop-top hard X-ray source appear in the MHD simulation.

Although the magnetic energy evolution is similar in both cases, the partitioning of the released magnetic energy into other forms would be different. Consider two MHD models with magnetic topologies and magnetic relaxation sequences similar to the two magnetofriction experiments. We expect that, in the MHD version of the magnetofriction periodic experiment, a relatively larger fraction of the released magnetic energy would be in the form of bulk kinetic energy associated with the eruption. In contrast, in an MHD version of the magnetofriction enclosed experiment, the eruption would be confined, and some of this kinetic energy would instead be converted into compressive work, causing adiabatic heating of the plasma, thereby enhancing downward transport by thermal condition, leading to increased chromospheric evaporation and radiative losses. So, apart from differences in the flare ribbon structure of long-range loops, one may expect the non-periodic system to yield a larger flare (in terms of peak X-ray flux). Still, both systems are expected to have a set of compact flare loops above the parasite bipole.

Data availability

We have opted not to make the MURaM code publicly available. The codebase is frequently updated, and running the code in an appropriate and efficient manner requires expert assistance. The numerical methods employed by the code are provided in detail in refs [17,50]. Interested parties are invited to contact the authors for more detailed information. Simulation snapshots are available for download from the Stanford Digital Repository (https://purl.stanford.edu/dv883vb9686). The repository also provides Interactive Data Language and Python routines for analysing the simulation data.

References

1. Priest, E. R. & Forbes, T. G. The magnetic nature of solar flares. *Astron. Astrophys. Rev.* **10**, 313–377 (2002).
2. Shibata, K. & Magara, T. Solar flares: magnetohydrodynamic processes. *Living Rev. Solar Phys.* **8**, 6 (2011).
3. Schrijver, C. J. Driving major solar flares and eruptions: a review. *Adv. Space Res.* **43**, 739–755 (2009).
4. Fisher, G. H. et al. The coronal global evolutionary model: using HMI vector magnetogram and Doppler data to model the buildup of free magnetic energy in the solar corona. *Space Weather* **13**, 369–373 (2015).
5. Amari, T., Canou, A. & Aly, J.-J. Characterizing and predicting the magnetic environment leading to solar eruptions. *Nature* **514**, 465–469 (2014).
6. Wyper, P. F., Antiochos, S. K. & DeVore, C. R. A universal model for solar eruptions. *Nature* **544**, 452–455 (2017).
7. Benz, A. O. Flare observations. *Living Rev. Solar Phys.* **5**, 1 (2008).
8. Caspi, A. & Lin, R. P. *RHESSI* line and continuum observations of super-hot flare plasma. *Astrophys. J. Lett.* **725**, L161–L166 (2010).
9. Fisher, G. H., Canfield, R. C. & McClymont, A. N. Flare loop radiative hydrodynamics. VI. Chromospheric evaporation due to heating by nonthermal electrons. *Astrophys. J.* **289**, 425–433 (1985).
10. Reeves, K. K., Warren, H. P. & Forbes, T. G. Theoretical predictions of X-ray and extreme-UV flare emissions using a loss-of-equilibrium model of solar eruptions. *Astrophys. J.* **668**, 1210–1220 (2007).
11. Longcope, D. W., Guidoni, S. E. & Linton, M. G. Gas-dynamic shock heating of post-flare loops due to retraction following localized, impulsive reconnection. *Astrophys. J. Lett.* **690**, L18–L22 (2009).
12. Takasao, S., Matsumoto, T., Nakamura, N. & Shibata, K. Magnetohydrodynamic shocks in and above post-flare loops: two-dimensional simulation and a simplified model. *Astrophys. J.* **805**, 135 (2015).
13. Kusano, K. et al. Magnetic field structures triggering solar flares and coronal mass ejections. *Astrophys. J.* **760**, 31 (2012).
14. Janvier, M., Aulanier, G. & Démoulin, P. From coronal observations to MHD simulations, the building blocks for 3D models of solar flares (invited review). *Solar Phys.* **290**, 3425–3456 (2015).
15. Kleint, L. et al. The fast filament eruption leading to the X-flare on 2014 March 29. *Astrophys. J.* **806**, 9 (2015).
16. Young, P. R., Tian, H. & Jaeggli, S. The 2014 March 29 X-flare: subarcsecond resolution observations of Fe XXI λ1354.1. *Astrophys. J.* **799**, 218 (2015).
17. Rempel, M. Extension of the MURaM radiative MHD code for coronal simulations. *Astrophys. J.* **834**, 10 (2017).
18. Archontis, V. & Török, T. Eruption of magnetic flux ropes during flux emergence. *Astron. Astrophys.* **492**, L35–L38 (2008).
19. Aulanier, G., Török, T., Démoulin, P. & DeLuca, E. E. Formation of torus-unstable flux ropes and electric currents in erupting sigmoids. *Astrophys. J.* **708**, 314–333 (2010).
20. Cheng, X., Zhang, J., Liu, Y. & Ding, M. D. Observing flux rope formation during the impulsive phase of a solar eruption. *Astrophys. J. Lett.* **732**, L25 (2011).
21. Nindos, A., Patsourakos, S., Vourlidas, A. & Tagikas, C. How common are hot magnetic flux ropes in the low solar corona? A statistical study of EUV observations. *Astrophys. J.* **808**, 117 (2015).
22. Yokoyama, T. & Shibata, K. Magnetohydrodynamic simulation of a solar flare with chromospheric evaporation effect based on the magnetic reconnection model. *Astrophys. J.* **549**, 1160–1174 (2001).
23. Reep, J. W., Bradshaw, S. J. & Alexander, D. Optimal electron energies for driving chromospheric evaporation in solar flares. *Astrophys. J.* **808**, 177 (2015).
24. Fletcher, L. & Hudson, H. S. Impulsive phase flare energy transport by large-scale Alfvén waves and the electron acceleration problem. *Astrophys. J.* **675**, 1645–1655 (2008).
25. Kowalski, A. F., Allred, J. C., Daw, A., Cauzzi, G. & Carlsson, M. The atmospheric response to high nonthermal electron beam fluxes in solar flares. I. Modeling the brightest NUV footpoints in the X1 solar flare of 2014 March 29. *Astrophys. J.* **836**, 12 (2017).
26. Del Zanna, G., Schmieder, B., Mason, H., Berlicki, A. & Bradshaw, S. The gradual phase of the X17 flare on October 28, 2003. *Solar Phys.* **239**, 173–191 (2006).
27. Milligan, R. O. & Dennis, B. R. Velocity characteristics of evaporated plasma using hinode/EUV imaging spectrometer. *Astrophys. J.* **699**, 968–975 (2009).
28. Jeffrey, N. L. S., Fletcher, L. & Labrosse, N. First evidence of non-Gaussian solar flare EUV spectral line profiles and accelerated non-thermal ion motion. *Astron. Astrophys.* **590**, A99 (2016).
29. Liu, W., Petrosian, V., Dennis, B. R. & Jiang, Y. W. Double coronal hard and soft X-ray source observed by *RHESSI*: evidence for magnetic reconnection and particle acceleration in solar flares. *Astrophys. J.* **676**, 704–716 (2008).
30. Krucker, S. & Battaglia, M. Particle densities within the acceleration region of a solar flare. *Astrophys. J.* **780**, 107 (2014).
31. Boris, J. P. *A Physically Motivated Solution of the Alfvén Problem* NRL Memorandum Report 2167 (Naval Research Laboratory, 1970).

32. Gombosi, T. I. et al. Semirelativistic magnetohydrodynamics and physics-based convergence acceleration. *J. Comput. Phys.* **177**, 176–205 (2002).

33. Gombosi, T. I., Jokipii, J. R., Kota, J., Lorencz, K. & Williams, L. L. The telegraph equation in charged particle transport. *Astrophys. J.* **403**, 377–384 (1993).

34. Snodin, A. P., Brandenburg, A., Mee, A. J. & Shukurov, A. Simulating field-aligned diffusion of a cosmic ray gas. *Mon. Not. R. Astron. Soc.* **373**, 643–652 (2006).

35. Rempel, M. Numerical simulations of quiet Sun magnetism: on the contribution from a small-scale dynamo. *Astrophys. J.* **789**, 132 (2014).

36. Judge, P. G., Kleint, L., Donea, A., Sainz Dalda, A. & Fletcher, L. On the origin of a sunquake during the 2014 March 29X1 flare. *Astrophys. J.* **796**, 85 (2014).

37. Yang, K., Guo, Y. & Ding, M. D. Quantifying the topology and evolution of a magnetic flux rope associated with multi-flare activities. *Astrophys. J.* **824**, 148 (2016).

38. Li, Y., Ding, M. D., Qiu, J. & Cheng, J. X. Chromospheric evaporation in an X1.0 flare on 2014 March 29 observed with IRIS and EIS. *Astrophys. J.* **811**, 7 (2015).

39. Rubio da Costa, F., Kleint, L., Petrosian, V., Liu, W. & Allred, J. C. Data-driven radiative hydrodynamic modeling of the 2014 March 29 X1.0 solar flare. *Astrophys. J.* **827**, 38 (2016).

40. Liu, C. et al. A circular-ribbon solar flare following an asymmetric filament eruption. *Astrophys. J. Lett.* **812**, L19 (2015).

41. Fan, Y. The emergence of a twisted flux tube into the solar atmosphere: sunspot rotations and the formation of a coronal flux rope. *Astrophys. J.* **697**, 1529–1542 (2009).

42. Manchester, W. B. IV Solar atmospheric dynamic coupling due to shear motions driven by the Lorentz force. *Astrophys. J.* **666**, 532–540 (2007).

43. Antiochos, S. K., DeVore, C. R. & Klimchuk, J. A. A model for solar coronal mass ejections. *Astrophys. J.* **510**, 485–493 (1999).

44. Lynch, B. J., Antiochos, S. K., DeVore, C. R., Luhmann, J. G. & Zurbuchen, T. H. Topological evolution of a fast magnetic breakout CME in three dimensions. *Astrophys. J.* **683**, 1192–1206 (2008).

45. Manchester, W. B. IV, Gombosi, T., DeZeeuw, D. & Fan, Y. Eruption of a buoyantly emerging magnetic flux rope. *Astrophys. J.* **610**, 588–596 (2004).

46. Jiang, C. et al. Data-driven magnetohydrodynamic modelling of a flux-emerging active region leading to solar eruption. *Nat. Commun.* **7**, 11522 (2016).

47. Hansteen, V. H., Hara, H., De Pontieu, B. & Carlsson, M. On redshifts and blueshifts in the transition region and corona. *Astrophys. J.* **718**, 1070–1078 (2010).

48. Cheung, M. C. M. & DeRosa, M. L. A method for data-driven simulations of evolving solar active regions. *Astrophys. J.* **757**, 147 (2012).

49. Cheung, M. C. M. et al. Homologous helical jets: observations by IRIS, SDO, and Hinode and magnetic modeling with data-driven simulations. *Astrophys. J.* **801**, 83 (2015).

50. Vögler, A. et al. Simulations of magneto-convection in the solar photosphere. Equations, methods, and results of the MURaM code. *Astron. Astrophys.* **429**, 335–351 (2005).

Author contributions

M.C.M.C. wrote code to synthesize and analyse remote sensing diagnostics from the numerical simulation, analysed SDO and IRIS data, managed the team of co-authors and contributed to writing the text. M.R. implemented the coronal extension of the MURaM radiative MHD code, conducted the MHD simulations, and contributed to data analysis and writing of the paper. G.C., M.L.D., V.H. and A.M. performed the analysis on the magnetic evolution of the simulated flare. F.C. performed the analysis on X-ray fluxes from the simulation. A.S.D. performed analysis on photospheric magnetic observables. P.T., B.D.P., M.C. and S.W.M. performed analysis on optically thin X-ray and EUV emission, and contributed to the text. J.M.-S. performed the analysis and wrote the text for the section on κ versus Gaussian distributions. M.C., B.G. and V.H. contributed to the extension of the numerical model to couple the convection zone with the atmosphere.

Competing interests

The authors declare no competing interests.

Additional information

Supplementary information is available for this paper at https://doi.org/10.1038/s41550-018-0629-3.

Reprints and permissions information is available at www.nature.com/reprints.

Correspondence and requests for materials should be addressed to M.C.M.C.

Publisher's note: Springer Nature remains neutral with regard to jurisdictional claims in published maps and institutional affiliations.